

Bubble-Based Microrobots with Rapid Circular Motions for Epithelial Pinning and Drug Delivery

Jin Gyun Lee, Ritu R. Raj, Cooper P. Thome, Nicole B. Day, Payton Martinez, Nick Bottenus, Ankur Gupta, and C. Wyatt ShieldsIV*

Remotely powered microrobots are proposed as next-generation vehicles for drug delivery. However, most microrobots swim with linear trajectories and lack the capacity to robustly adhere to soft tissues. This limits their ability to navigate complex biological environments and sustainably release drugs at target sites. In this work, bubble-based microrobots with complex geometries are shown to efficiently swim with non-linear trajectories in a mouse bladder, robustly pin to the epithelium, and slowly release therapeutic drugs. The asymmetric fins on the exterior bodies of the microrobots induce a rapid rotational component to their swimming motions of up to ≈ 150 body lengths per second. Due to their fast speeds and sharp fins, the microrobots can mechanically pin themselves to the bladder epithelium and endure shear stresses commensurate with urination. Dexamethasone, a small molecule drug used for inflammatory diseases, is encapsulated within the polymeric bodies of the microrobots. The sustained release of the drug is shown to temper inflammation in a manner that surpasses the performance of free drug controls. This system provides a potential strategy to use microrobots to efficiently navigate large volumes, pin at soft tissue boundaries, and release drugs over several days for a range of diseases.

1. Introduction

Engineered nanoparticles are effectual drug carriers due to their ability to protect drugs from degradation, durability within the body, high surface area-to-volume ratios, and control over drug release rates.^[1–5] However, many nanoparticle systems rely on circulation or diffusion as their primary mode of transport, which limits their ability to reach specific tissues.^[6–8] Previous reports show that nanoparticles administered in the

body face both physical and biological barriers that limit their accumulation in diseased tissues.^[9] Moreover, the persistence of nanoparticles at tissue boundaries is often limited since the adsorption of nanoparticles weakens upon decreasing particle diameter.^[10] Poor adhesion consequently decreases the retention of nanoparticles and hinders sustained drug release in vivo, limiting the usefulness of many nanoparticle-based drug delivery systems in clinical settings.^[11]

In nature, biological swimmers, such as microorganisms and sperm, often traverse complex environments within non-linear motions to enhance motility.^[12–14] Depending on the unique shape of the cell or organism, they adopt swimming behaviors along 3D trajectories in biological fluids, which promote navigation and survival of the microorganism.^[15,16] For example, *Escherichia coli* are known to swim in circular motions by the action


of rotary motors embedded in the cell wall to enhance the probability of adhesion to the surface.^[12] Inspired by the biological swimmers in nature, self-propelling particles are synthetic analogs that can mimic the motions of natural swimmers in biological fluids. Recently, the self-propelling particles have garnered considerable attention as medical microrobots in the field of biomedical engineering due to their ability to swim to hard-to-reach tissues and deliver drugs or genes at target sites.^[17–20]

In contrast to passive nanoparticles, microrobots can efficiently traverse viscous fluids by breaking surface symmetry to locally dissipate energy.^[21–25] Common sources of energy to power microrobots include chemical reactions,^[26,27] magnetic fields,^[28–32] electric fields,^[33–36] and acoustic fields.^[37–39] Among these, acoustic fields are particularly promising for in vivo use due to the biocompatibility and clinical availability of ultrasound.^[40,41] Recent studies report that acoustically powered microrobots with an internal cavity can self-propel by the oscillation of an entrapped air bubble at its resonant frequency.^[39,42] Previously reported bubble-based microrobots have been shown to travel through microchannels^[37] and transport cells in vitro;^[43] however, challenges remain to using bubble-based microrobots for drug delivery. Principally, microrobots should: 1) propel with non-linear directionality to enhance navigation through tortuous biological environments, 2) move with ample thrust to penetrate dense or viscous biological barriers and

J. G. Lee, R. R. Raj, C. P. Thome, N. B. Day, A. Gupta, C. Wyatt Shields
Department of Chemical and Biological Engineering
University of Colorado Boulder 3415 Colorado Ave
Boulder, CO 80303, USA
E-mail: charles.shields@colorado.edu

P. Martinez, N. Bottenus
Department of Mechanical Engineering
University of Colorado Boulder
1111 Engineering Drive, UCB 427, Boulder, CO 80309, USA

P. Martinez, N. Bottenus, C. Wyatt Shields
Biomedical Engineering Program
University of Colorado Boulder
1111 Engineering Drive, UCB 422, Boulder, CO 80309, USA

 The ORCID identification number(s) for the author(s) of this article can be found under <https://doi.org/10.1002/sml.202300409>.

DOI: 10.1002/sml.202300409

mechanically pin themselves to tissue substrates, and 3) facilitate the slow release of drugs to sustain therapeutic benefits in vivo.^[44,45]

We present a bubble-based, acoustically powered, polymeric microrobot that can swim at high speeds (≈ 150 body lengths per second), rapidly navigate aqueous environments, securely pin themselves at soft tissue boundaries, and sustainably release small molecule drugs at tissue boundaries to promote sustained therapeutic effects. We designed the microrobots with a cavity in their central compartment to entrap an air bubble when submerged in aqueous fluids. Under an acoustic traveling wave at the frequency at the maximal acoustic response of the bubble (320 kHz), the bubble oscillates by stable cavitation, creating fluid flows away from the air/liquid interface, which drives the self-propulsion of the microrobot. To reliably generate non-linear directionality upon acoustic excitation, we introduced both symmetric and asymmetric fins on the bodies of the microrobots, which gave rise to rotational and orbital motions, respectively. The incorporation of fins gives rise to ultrafast motions (≈ 150 body lengths or ≈ 2.8 mm per second), which is notably faster than that of microrobots powered by other means such as magnetic fields or catalytic reactions. Further, we encapsulated the drug, dexamethasone (DEX), into the polymeric matrix of the microrobots and showed its sustained release over several days. To demonstrate the usefulness of the microrobots with asymmetric fins, we showed that they can self-propel within a mouse bladder *ex vivo* and mechanically pin themselves along the bladder epithelium. We show that DEX released from the microrobots can sustainably polarize primary macrophages *in vitro* toward an anti-inflammatory (or M2-like) phenotype, which supports its potential to be used as an immunotherapy for inflammatory diseases such as interstitial cystitis.^[46] Our study highlights a new method of active drug delivery that leverages the rapid and non-linear directional propulsion of microrobots to efficiently travel large distances within organs and sustainably release drugs to diseased tissues.

2. Results and Discussion

2.1. Fabrication and Characterization of Drug-Loaded Microrobots

To assess their therapeutic potential, we designed microrobots to treat interstitial cystitis. Interstitial cystitis is a chronic disorder of the bladder that causes discomfort, pelvic pain, frequent urination, and sometimes the appearance of blood in the urine.^[47] Currently, the most common treatment for interstitial cystitis is bladder instillation, whereby DEX dissolved in a solution of dimethyl sulfoxide (DMSO) is administered to the bladder and eventually drained using a catheter.^[46] Patients must hold the solution in their bladder for 15–20 min, which is painful for patients and limits drug effectiveness due to the low residence time of the drug.^[48] Thus, we encapsulated DEX into the polymeric bodies of the acoustically powered microrobots such that they could propel within the bladder upon stimulation by ultrasound, securely attach to the bladder epithelium, and slowly release the drug for several days.

DEX was encapsulated within the microrobots by dissolving it directly into the photoresist prior to 3D-crosslinking by two-photon lithography (Figure 1A–D and Movie S1, Supporting Information). DEX is an appropriate model drug due to its precedence in treating interstitial cystitis and other inflammatory diseases through its ability to heal damaged tissues by polarizing macrophages toward anti-inflammatory phenotypes.^[49] The hydrophobic nature of DEX allows it to readily dissolve into the photoresist, such that it can be slowly released into solution after microrobot fabrication and submersion in solution.

The microrobot was designed as an elongated half sphere with a diameter of 20 μm and a spherical cavity in its center (Figure 1E,F). The size of the microrobot and bubble was selected to eliminate the effects of buoyancy when the microrobot is suspended in solution. We found that spherical cavities larger than 11 μm for the given particle design resulted in microrobots floating at the air/liquid interface, causing the particles to assemble into clusters. Therefore, a cavity diameter of 11 μm was selected. Furthermore, we designed three curved fins on the bodies of the microrobots to generate torque at the single-particle level (Figure 1G,H). Microrobots with three symmetric fins, that is, all fins had the same shape and were evenly placed around the robot, rotated on the substrate upon application of the acoustic field. When one of the fins was smaller than the other two, the microrobots swam in an orbital motion along a circular path while the microrobots without fins moved randomly (Figure 1I). While our study focuses on the directed transport of microrobots in the bladder, which is a simple organ in terms of its geometry, designing microrobots to propel with non-linear trajectories (i.e., superimposed locomotive modes of transitional, rotational, and orbital motions) could improve their navigation through more complex biological environments. Moreover, the sharp fins on the microrobots can enhance their mechanical pinning along tissue boundaries in the body, thus enabling the controlled release of drugs for enhanced therapeutic effects (Figure 1J).

2.2. Characterization of the Air Bubble Frequency at Maximal Acoustic Response and Microrobot Trajectory

To characterize the frequency at the maximal acoustic response of the air bubbles within the microrobots, we measured the acoustic pressure by frequency sweep tests in a glass chamber with a transducer (Figure S1, Supporting Information). Once the chamber was filled with an aqueous solution of phosphate-buffered saline (PBS), the air was immediately entrapped in the mushroom-like cavities of the microrobots (Figure 2A inset) to form air bubbles, and the air/liquid interface was stabilized by surface tension. Upon generating the acoustic traveling waves, the acoustic pressure at each frequency was recorded by a transducer submerged in PBS. In Figure 2A, the harmonic cavitation dose is shown as a function of applied frequency. Here, the frequency at maximal acoustic response is expected to depend on the diameter of the spherical cavity as well as the diameter of the orifice at the air/liquid interface. Prior work has shown that decreasing the size of the cavity results in an increased resonance frequency.^[38,39,42] Aside from resonance

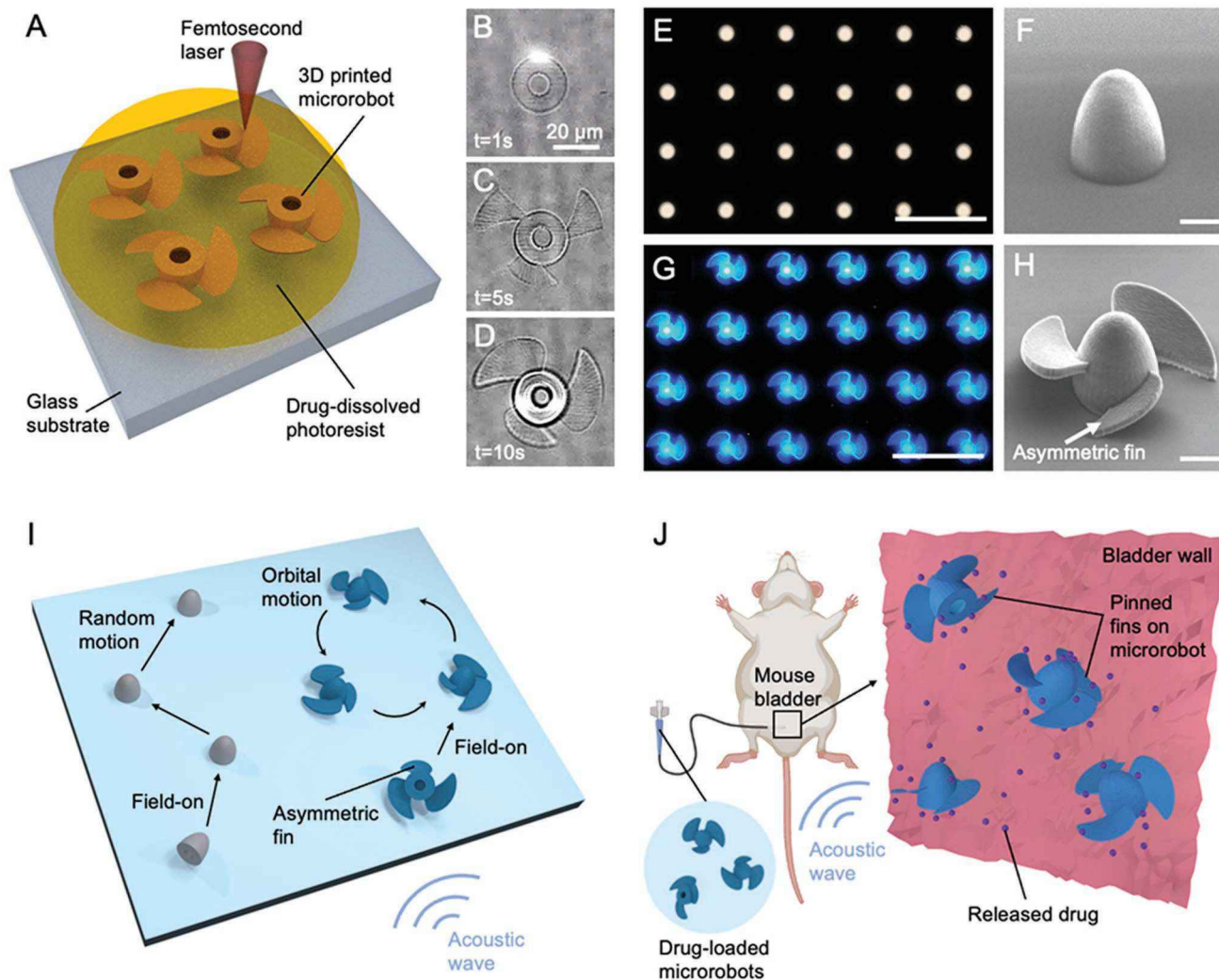


Figure 1. Fabrication, propulsion, and pinning of the acoustically powered microrobots for sustained drug release. A) Schematic illustration for the 3D-printing of drug-loaded microrobots with individual air bubbles using two-photon lithography. B–D) Images showing the 3D printing of a single microrobot. Small molecule drugs are encapsulated within the polymer matrix of the microrobots during their cross-linking. E) Fluorescent microscope and F) SEM images of a microrobot without fins. G) Fluorescent microscope and H) SEM images of a microrobot with asymmetric fins. I) Schematic illustration describing the effect of asymmetric fins on propulsion trajectories. Upon applying ultrasound, microrobots flip on the substrate due to microstreaming flows near the air/liquid interface of the bubbles. The microrobot with asymmetric fins propels in an orbital motion while the microrobot without fins propels in a random motion. J) Illustration of drug-loaded microrobots tempering an inflammatory response in bladder tissue. Upon excitation by ultrasound, the bubble-based microrobots travel through a mouse bladder until encountering the bladder wall. Fins on the microrobots improve their pinning against the wall, whereupon the drug is gradually released to sustainably treat immune cells. Scale bars in (E) and (G) = 100 μm . Scale bars in (F) and (H) = 10 μm .

and buoyancy effects, the propulsive force generated by the bubble oscillations also scales with the cavity size.^[42] To ensure negative buoyancy and maximal propulsive force, we designed microrobots with a spherical cavity diameter of 11 μm and an orifice diameter of 7.4 μm . For this design, we determined the maximal acoustic response to be at 320 kHz, which yielded a peak harmonic cavitation dose of $2.0 \times 10^{-4} \text{ V}^2$.

To stimulate the air bubble in microrobots with an acoustic traveling wave, a silicone spacer was placed between the transducer and the sensor to form a fluidic chamber (Figure 2B). PBS was used as the propulsion medium to simulate a physiologically relevant environment; notably, using PBS

also increased the stability of the air bubble due to increased surface tension. To introduce the acoustic field, a sinusoidal AC signal was applied to the piezoelectric transducer adjacent to the silicone spacer. Upon application of the acoustic field, the microrobots reorient such that the air/liquid interface of the air bubble is parallel to the substrate. This reorientation is attributed to secondary Bjerknes forces, which are attractive between the air bubble and the substrate.^[42,50,51] Microrobots with symmetric fins swim with a linear slipping motion of transitional speed, v_t , driven by primary acoustic radiation forces from the transducer.^[42] While the microrobot slips along the surface, we observed that its body rotates with an angular

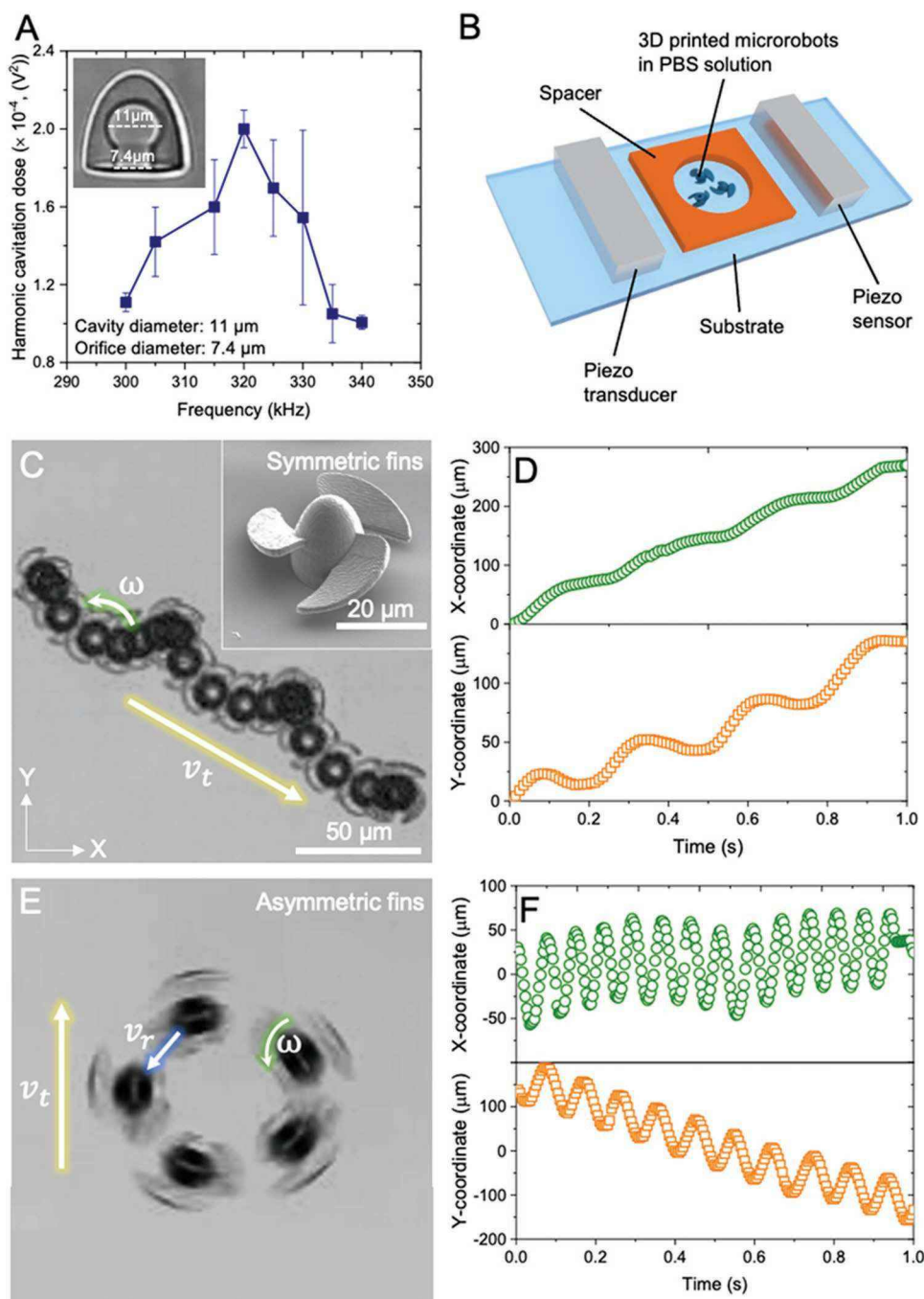


Figure 2. Characterization of air bubble frequency at the maximal acoustic response and microrobot trajectories. A) Dependence of the harmonic cavitation dose on frequency. (Inset) Image showing the geometry of a microrobot with a cavity diameter of $11 \mu\text{m}$ and an orifice diameter of $7.4 \mu\text{m}$. The frequency at maximal acoustic response is found at 320 kHz . B) Schematic illustration showing an experimental setup for acoustic propulsion. A transducer and a sensor are glued to a glass slide, and a silicone spacer is attached adjacent to the transducer. Microrobots in PBS are introduced into the fluidic chamber. C) Superimposed optical microscope image of a microrobot with symmetric fins. The microrobot with symmetric fins swims in a rotational motion with angular velocity (ω) and translational velocity (v_t). (Inset) SEM image showing the geometry of a microrobot with symmetric fins. D) Displacement of the microrobot with symmetric fins as a function of time. E) Superimposed optical microscope image of a microrobot with asymmetric fins. The microrobot with asymmetric fins swims in an orbital motion with ω , tangential speed (v_r), and v_t . F) Displacement of the microrobot with asymmetric fins as a function of time.

velocity, ω , counterclockwise (Figure 2C,D). When microrobots have one fin that is smaller than the other two, they experience both rotational and orbital motions along a circular path

with a tangential speed, v_r , with the smaller fin facing toward the center of the orbit (Figure 2E,F and Movie S2, Supporting Information).

2.3. Streaming Flows and Fluid Patterns Near the Microrobot

To understand the origins of the rotating and orbital motion of the microrobots with asymmetric fins, we performed numerical simulations and experiments with tracer particles. We propose two complementary explanations: 1) the streaming flows generated by the oscillating bubble interact with the asymmetric fins, leading to asymmetry in the flows and consequently rotation; and 2) the fins themselves vibrate and cause asymmetry in the streaming flows, as inspired by recent works showing that the acoustic response of solid structures generates steady streaming flows.^[52]

From our experimental results, we observed that the trajectory of microrobots is governed by their shape (Figure 3A). We observed fluid being ejected from the bottom of the microrobots, which causes a propulsive force in the positive *z*-direction. To determine the interaction between the fin- and bubble-generated streaming flows, we conducted numerical simulations of the flows generated by the oscillating air/liquid interface (Figures S2 and S3, Supporting Information). For a side view of the streaming flows, we sliced the *yz*-plane cross section at the center of each microrobot (Figure 3B) to visualize the time-averaged second-order velocity and pressure fields without the inclusion of quiescent and first-order fields (Figure 3C–E). The streaming flow of each microrobot from a top-down view was visualized in a similar fashion by slicing a *xy*-plane cross-section (Figure 3F). In our experiments, the presence of a substrate causes an attractive force that balances the propulsive force caused by fluid ejection, leading the microrobots to point upward at the substrate.^[53] In Figure 3G, we show that the fluid flows and pressure field are symmetric about the *z*-axis. This agrees with our experimental results, as no rotational or orbital motion is observed for microrobots without fins. Figure 3D,H shows the same time-averaged flows and pressure field for a microrobot with symmetric fins. In Figure 3D, we see that the streamlines rotate about the microrobot. However, the flows are still symmetric about the *z*-axis, which is in an agreement with our experimental results, as a microrobot with symmetric fins experiences rotation but no orbital motion. Figure 3E,I shows the time-averaged flows and pressure field for microrobots with asymmetric fins. We still observe a rotational component in the flow; however, the flows are no longer symmetric about the *z*-axis. The rotation and asymmetry in the streaming flows corroborate our experimental observations that microrobots with asymmetric fins swim in both rotational and orbital motions.

To visualize the fluid flow around structures driven solely by the oscillation of fins without any streaming flow from the air bubble, microrobots with different fin designs—but lacking a cavity—were printed on cylindrical posts (Figure 3J,K). We actuated the fins on the microrobots in a quiescent fluid environment at a frequency of 320 kHz and visualized the induced streaming flows using polystyrene (PS) tracer spheres (diameter = 0.75 μm) suspended in the fluid (Figure S4 and Movie S3, Supporting Information). We observed tracer particle motion without the presence of a bubble in the particle, indicating that the fins are responding to the acoustic field and generating a net streaming flow. As shown in Figure 3K, we recorded the motion of the tracer particles around immobilized microrobots while the field was applied. Then, to visualize the side-view

fluid pattern, we superimposed each frame of the captured videos to yield a single image showing the paths of tracer particles in the fluid. Similarly, Figure 3L,M shows superimposed top-down views of tracer particle movement in response to acoustic field application for microrobots with symmetric fins and asymmetric fins, respectively. We observed that the tracer particles moved around the microrobots and that microrobots with asymmetric fins also showed asymmetry in the motion of tracer particles in the imaging plane (Movie S4, Supporting Information). Because we observed tracer particle motion without the presence of an air bubble, we surmised that the fins are also responding to the acoustic field by independently generating net streaming flows. We believe that this observation is a result of the acoustic streaming generated by the vibration of thin structures.^[54,55] By extension, the streaming flows generated by the fins in response to the acoustic field could also be responsible for the rotational and orbital motion of the microrobots with bubbles. Thus, the streaming flows generated by the: 1) acoustically actuated bubble interacting with the fins and 2) vibration of the fins themselves provide explanations for the rotation and circular trajectories we observe. That is, the addition of external structures to influence the locomotion of acoustically actuated particles may lead to effects that are not solely due to interactions between bubble-generated flow and the external structures but also include effects generated by the acoustic vibration of the structures. We believe that the interplay between these disparate effects can give rise to a rich diversity of the motions of acoustically actuated microrobots, especially when driven by different applied frequencies that selectively excite the bubble or the external structures. To elucidate the relative contribution of the oscillating air bubble with respect to the vibrating fins on the resultant motion of microrobots, additional studies are necessary.

2.4. Mechanical Pinning of Microrobots with Asymmetric Fins

In Figure 4A, we show that the speed (measured in body lengths per second) of microrobots linearly increases with the square of the applied voltage. Here, the body length of microrobots is equivalent to the major radius or the minor diameter of the hemi-ellipsoidal shape of a microrobot, both of which are 20 μm (Figure S5, Supporting Information). We expect the speed to continue increasing with applied voltage up to an experimental limit, that is, from heating or amplification considerations, or a physical limit, that is, a transition from stable to inertial cavitation due to an increased applied pressure amplitude.^[56] At the maximum applied voltage tested, we observed that microrobots with asymmetric fins propelled at a tangential speed of 2855 $\mu\text{m s}^{-1}$ (143 body lengths per second). We note that this speed is significantly faster than the speed of particles stimulated by other means, such as 1) Janus particles in AC electric fields^[33] or in catalytic solutions^[57] (e.g., ≈ 5 –10 body lengths per second) and 2) helical microrobots under magnetic fields (e.g., ≈ 35 body lengths per second).^[58] The ultrafast speed of acoustic microrobots may be useful for penetrating biological barriers or enhancing the delivery of drugs in vivo.

To facilitate sustained activation of immune cells, it is important to maximize the retention of drug-loaded microrobots at

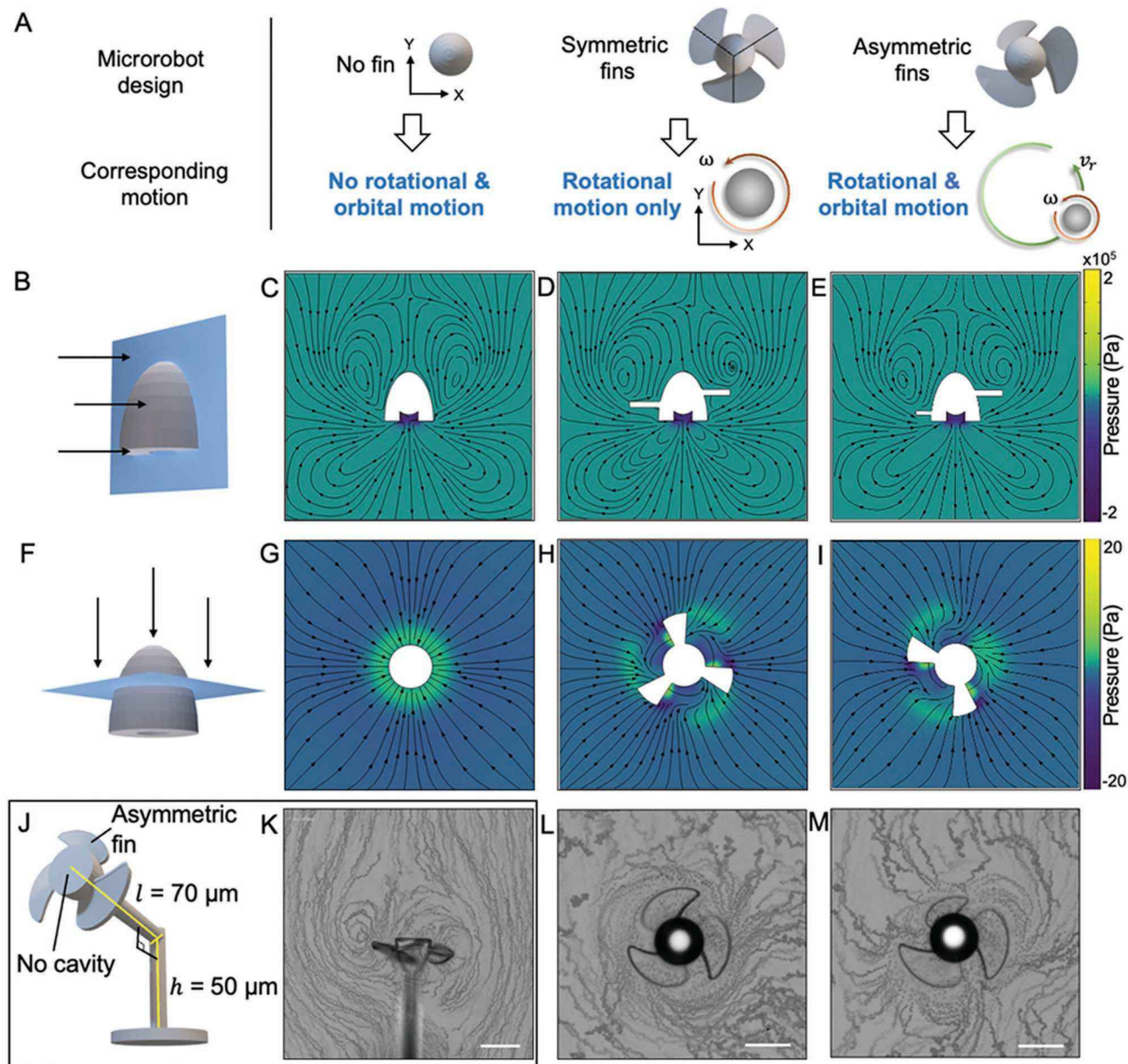


Figure 3. Numerical simulations of streaming flows and empirically observed fluid patterns for the microrobots. A) Schematic illustration of microrobot designs and corresponding motions under acoustic excitation. Microrobots without fins do not experience rotational or orbital motion. Microrobots with symmetric fins only rotate. Microrobots with asymmetric fins experience both rotational and orbital motions. B–E) Schematic illustration of the B) yz -plane sliced on simulation results for microrobots with C) no fins, D) symmetric fins, and E) asymmetric fins. F–I) Schematic illustration of the F) xy -plane sliced on simulation results for microrobots with G) no fins, H) symmetric fins, and I) asymmetric fins. Black lines and arrows in the streaming patterns represent the simulated streamlines of the time-averaged second-order streaming flows around the microrobots, which ignore quiescent and first-order pressure fields. The colors represent the corresponding time-averaged second-order pressure fields around the microrobots. J) Model design of a 3D-printed microrobot with asymmetric fins and without a cavity immobilized on a post for visualizing the side view of the microrobots. K) Superimposed image of the experimental fluid patterns around the microrobots from the structure shown in (J) under an acoustic field of 320 kHz. Superimposed image of the experimental fluid patterns around microrobots without a cavity and with L) symmetric fins and M) asymmetric fins from a top-down view under an acoustic field of 320 kHz. Scale bars = 20 μm .

target sites. To investigate the role of fins on the attachment of microrobots, we studied their pinning at the wall of a silicone chamber as a surrogate bladder. We examined different designs of particles across a range of applied voltages. We measured the fraction of particles pinned on the silicone wall

by counting the remaining particles after washing the chamber and dividing by the total number of particles injected. Upon applying a 320 kHz acoustic wave, microrobots with air bubbles translocated to the wall of the silicone chamber due to primary acoustic radiation forces, while the PS spheres without air

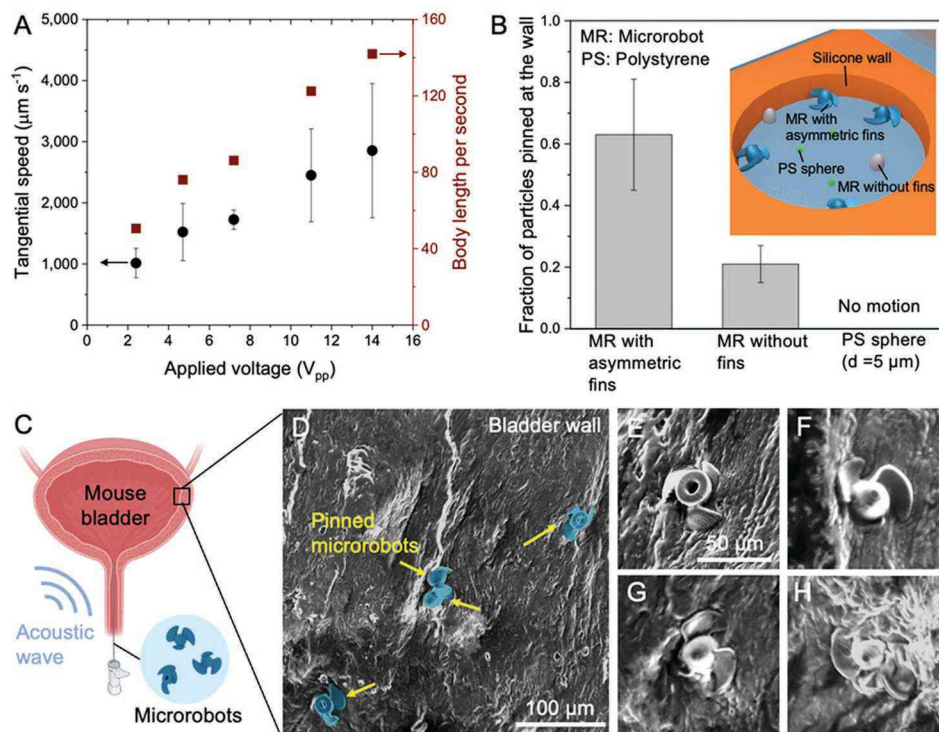


Figure 4. Pinning of microrobots on the bladder wall. A) Tangential speed of microrobots as a function of applied voltage. B) Fraction of particles pinned on the silicone wall with different particle designs. Inset: schematic representation showing the experimental setup with different types of particles. Particles remaining on the wall were counted after applying the acoustic field and washing the chamber. C) Schematic illustration of an ex vivo experiment of microrobot propulsion in a mouse bladder. D–H) SEM images showing pinned microrobots on the mouse bladder wall. Due to the smaller contact area between the sharp fins on the bodies of the microrobots and the wall, the larger pressures acting on the microrobots resulted in better pinning.

bubbles did not exhibit any motion as expected. To simulate the shear stresses experienced by urination in the bladder (average flow rate of urine from a mouse is $\approx 1 \text{ mL min}^{-1}$),^[59] the fluid inside of the chamber was aspirated using a syringe, and fresh PBS was introduced into the chamber and aspirated again at a flow rate of 1.5 mL min^{-1} . After washing the chamber, we observed that microrobots with asymmetric fins remained pinned (Figure 4B). When not pinned, microrobots, as well as PS spheres, were easily washed out from the chamber.

To investigate the pinning behavior of microrobots to a bladder epithelium, we performed ex vivo experiments on the bladders of C57BL/6J mice. Bladders were extracted from euthanized mice, and microrobots with asymmetric fins were dispersed in PBS and infused into the bladders (Figure 4C). After applying an acoustic field to the bladders, we observed the pinning of microrobots at the bladder walls using fluorescent microscopy and scanning electron microscope (SEM) (Figure S6A–C, Supporting Information). In Figure 4D–H, the SEM images show that the microrobots are pinned at the bladder wall with the fins partially inserted in the epithelium. The high fraction of microrobots with fins pinned at the wall may be attributed to two reasons: 1) the speed of the bubble-based microrobot is fast (in the range of mm per second), resulting in increasing kinetic energy exerted during collision, and 2) the large pressure acting on the wall due to the sharp edge of fins (Movie S5, Supporting Information). Since the fin has a small area of contact with the bladder, microrobots with fins can exert

greater pressure on the wall compared to that of microrobots without fins (Figure S6D, Supporting Information). To better understand the mechanism of pinning, future studies examining the influence of fin edge thickness, particle speed, and orientation upon pinning are necessary.

2.5. In Vitro Macrophage Polarization by Drug Release from Microrobots

For improving the efficacy of delivered drugs using engineered materials: 1) the materials used for drug delivery should have a long retention time at the target site^[60] and 2) the drug should be gradually released over time.^[61–64] After demonstrating the former by the non-linear directional propulsion of microrobots and their subsequent pinning on epithelial tissues, we sought to confirm that DEX-loaded microrobots can sustainably activate immune cells by controlled drug release. To do so, we measured the cumulative release of the drug from the microrobots and estimated the drug-loading capacity of a single microrobot. **Figure 5A** shows that the drug is gradually released from the polymer matrix over 6 days. To understand the kinetics of drug release, we fit the experimental data to the Korsmeyer–Peppas model for drug release

$$\frac{c_t}{c_\infty} = kt^n \quad (1)$$

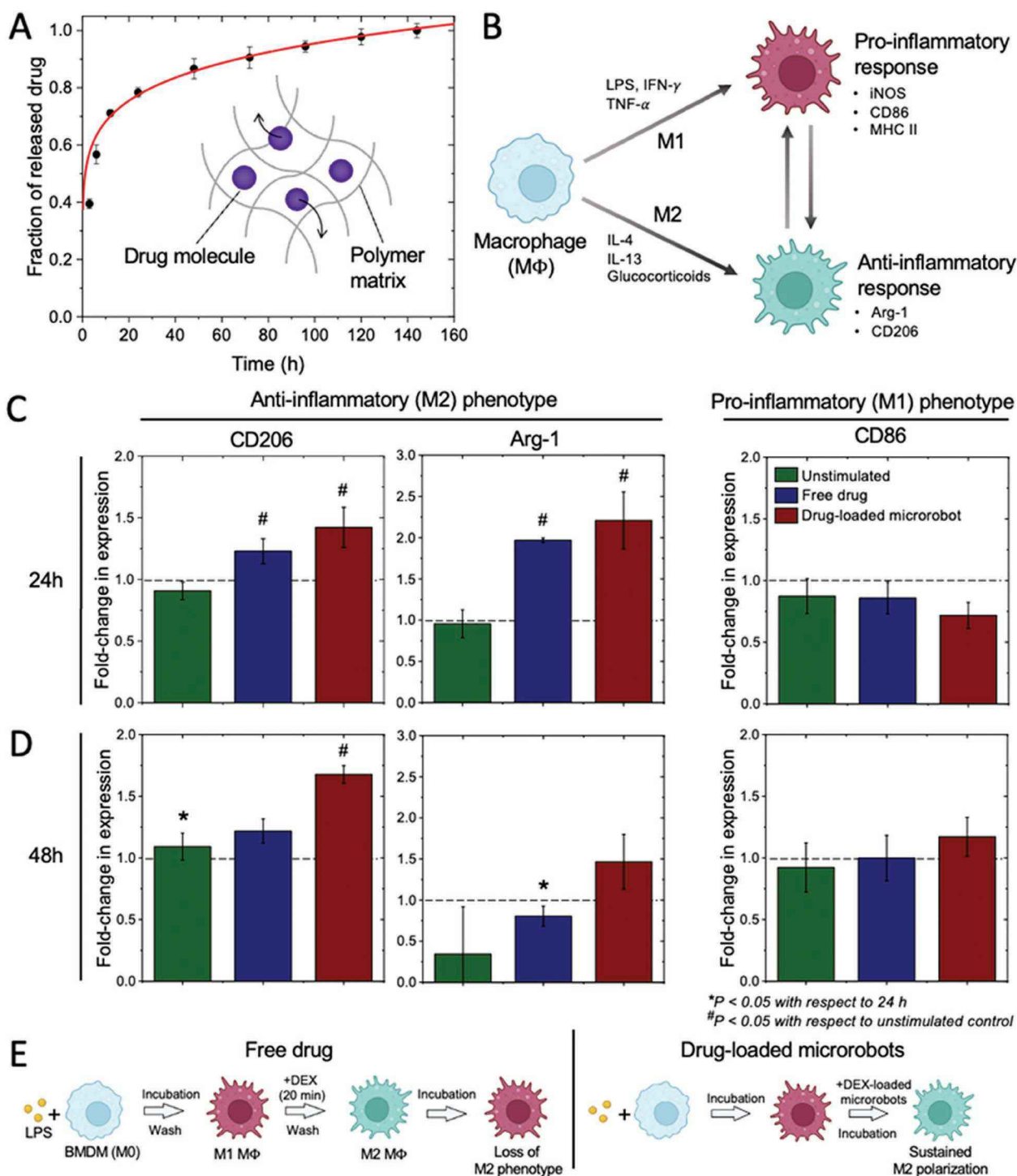


Figure 5. Macrophage phenotypic response to drug release from microrobots. A) Cumulative release of drug in 5 vol% DMSO solution at 37 °C over 6 days. The scatter points represent experimental data ($N = 3$), and the continuous line represents the best fit using a Korsmeyer–Peppas model. (Inset) Illustration describing the diffusion of DEX molecules through the polymer matrix of the microrobots. B) Illustration of phenotypic responses of macrophages. Macrophages can be polarized toward proinflammatory (M1) or anti-inflammatory (M2) phenotypes in response to signals from their environment. C,D) Macrophage responses to no stimulation, 20 min incubation with free drug, and drug-loaded microrobots, as measured by the change in the relative expression of M2 markers (CD206 and Arg-1) and an M1 marker (CD86) after C) 24 h and D) 48 h. The fold-change in the expression of M2 markers for macrophages incubated with 20 min of free drug drops after 48 h, while macrophages with drug-loaded microrobots maintained their increased expression. The statistical significance was determined using multiple unpaired, equal variance t -tests at the cutoff point $*p < 0.05$ and $\#p < 0.05$. E) Schematic illustration describing macrophage polarization by free drug and drug-loaded microrobots. Due to the short residence time of the drug, macrophages incubated with free drug lost their M2 phenotypes after 48 h, while macrophages incubated with drug-loaded microrobots maintained their M2 phenotypes for at least 48 h.

where $\frac{c_t}{c_\infty}$ is the fractional drug release at time t , k is the rate constant, and n is the release exponent.^[65,66] The Korsmeyer–Peppas model is a power law model that was developed to describe the release of small molecule drugs from a polymeric matrix.^[66] For drug release from polymeric particles, the rate of drug release is strongly governed by the crosslink density of particles, as well as the size of the molecule.^[67] In our study, the relatively fast release of DEX molecules within 6 days (90% release in 48 h) is attributed to the nature of DEX, a small molecule drug, as well as the low crosslink density of acrylate polymer, when printed using two-photon polymerization. We expect that this rate can be tuned by controlling the crosslink density of the polymer or the size of the encapsulated drug.

To confirm that the controlled release of DEX from the microrobots can treat immune cells better than the addition of free DEX acting as a bolus, we studied the extent to which the inflammatory phenotypes of primary murine macrophages were attenuated. Macrophages are specialized innate immune cells that help maintain tissue homeostasis and resist pathogen invasion in the body. The phenotype of macrophages changes depending on their microenvironment and can be ostensibly classified as proinflammatory (M1-like or “M1” for convenience) or anti-inflammatory (M2-like or “M2” for convenience).^[68] For example, lipopolysaccharide (LPS), interferon (IFN)- γ , and tumor necrosis factor (TNF)- α polarize macrophages toward M1 phenotypes. Conversely, interleukin (IL)-4, IL-13, and glucocorticoids polarize macrophages toward M2 phenotypes.^[69] Inflammatory diseases, such as interstitial cystitis, are triggered by the perturbation of tissue homeostasis, and monocytes that circulate in the bloodstream accumulate in the inflammation site and differentiate into macrophages.^[70] These and other tissue-resident macrophages are polarized toward an M1 phenotype. An imbalance of M1 and M2 macrophages may result in pathological consequences and cause inflammatory diseases.^[71] Therefore, anti-inflammatory treatments that promote the switching of M1 macrophage phenotypes toward M2 phenotypes can abate inflammation and repair damaged tissues (Figure 5B).

To temper macrophage inflammation, we first polarized macrophages toward an M1 state using 100 nm of LPS in Dulbecco’s modified Eagle’s medium (DMEM) (Figure 5B).^[72–74] We then examined the degree to which macrophages shifted toward M2 phenotypes after incubation with free DEX in a solution of DMSO administered for 20 min, according to clinical methods, or incubation with DEX-loaded microrobots. The total concentration of drug released from the microrobots over the incubation period was estimated to be equivalent to the total drug concentration administered for 20 min. Figure 5C,D shows the change in the expression of phenotypic markers relative to that of macrophages incubated with empty microrobots, to account for any potential effects from the material of the microrobots. The markers examined in this study include CD206 and arginase (Arg)-1 (known M2 markers) and inducible nitric oxide synthase (iNOS), CD86, and major histocompatibility complex (MHC) II (known M1 markers).^[75]

We found that macrophages incubated with free DEX for 20 min, as well as drug-loaded microrobots, showed an increase in expression of CD206 after 24 h, while no M1 markers showed

significant changes in expression (Figure S7, Supporting Information). After 48 h, macrophages that received 20 min of incubation with the free drug showed a reduced fold-change in the expression of CD206 from 1.3 to 1.1. On the other hand, the fold-change in the expression of CD206 on macrophages incubated with drug-loaded microrobots for 48 h increased to nearly 1.6. Thus, macrophages incubated with drug-loaded microrobots experienced a larger and more durable phenotypic shift compared to controls, which is attributed to the gradual release of DEX from the polymer matrix, whereas macrophages exposed to 20 min of free drug mostly lost their M2 phenotype by 48 h (Figure 5E).

3. Conclusion

We present an acoustically powered microrobot with asymmetric fins and describe their motion in 2D. When the microrobots are energized by an acoustic field at the frequency of the maximal acoustic response of the entrapped air bubble, the anisotropic fins cause the microrobots to rotate and experience orbital motion along circular trajectories. The combination of the high speed of microrobots and the sharp edges of the fins enables their robust pinning at soft boundaries, which we demonstrated *in vitro* and *ex vivo* in a mouse bladder, enhancing their residence time. Due to the strong forces exerted by the microrobots on soft epithelial tissues during pinning, further studies are needed to evaluate tissue responses using cell viability and gene expression assays in *in vivo* experiments. Additionally, we encapsulated the drug into the polymeric matrix of the microrobots by dissolving it into the photoresist for sustained release. Using DEX as a model immunomodulatory drug, we showed that >90% of DEX in the microrobots can be released by diffusion within 2 days. This gradual release of DEX polarizes macrophages better than free drug, resulting in a sustained M2 phenotype over 48 h, while macrophages exposed to 20 min of free DEX lost their phenotype after 48 h. The microrobots shown herein have the potential for treating interstitial cystitis and a range of other diseases that require the efficient transport of drugs across large, viscous, or tortuous biological areas for controlled release.

4. Experimental Section

Fabrication of Drug-Loaded Microrobots with Air Bubbles: Microrobots were 3D-printed on a fused silica substrate via two-photon polymerization (Photonic Professional GT2, Nanoscribe GmbH) using a 63 \times objective lens and IP-Dip photoresist, which is known to be non-toxic and bioinert.^[76,77] The 3D microprinting was performed with a laser power of 40 mW and a galvanometric mirror with an x - and y -scanning speed of 20 mm s⁻¹. DEX (MedChemExpress) was encapsulated by dissolving 1 mg DEX powder into 1 g photoresist. Above this concentration of DEX in the photoresist, 3D printing could not be initiated due to undissolved DEX hindering the detection of the substrate-photoresist interface. Drug-loaded microrobots were then developed in SU-8 developer (MicroChem Corp.) for 30 min to remove uncrosslinked photoresist and washed in isopropyl alcohol for 5 min. The removal of the photoresist and the existence of air bubbles in the microrobots were confirmed by the propulsion experiments, as well as frequency sweep tests (Figure 2).

Microrobot Imaging and Tracking: To characterize microrobot geometry and printing resolution, particles on a silica substrate were

sputter-coated with platinum (thickness = 20 nm) and imaged with an SEM in a secondary electron imaging modality at an accelerating voltage of 10 kV (Hitachi SU3500). The rapid dynamics of the microrobots under an acoustic field were recorded by a Nikon Widefield microscope equipped with a Hamamatsu ORCA-FLASH4.0 V3 digital CMOS camera with a frame rate of 200 frames s⁻¹. The coordinates of the swimming microrobots were extracted using ImageJ software.^[78,79] Each frame of the video was converted to a binary image, and the position of each microrobot was tracked using the “Centroid” function in “Analyzer Particles.” The tangential speed of microrobots was determined with asymmetric fins by calculating the average distance and time required for the microrobots to complete one revolution. The fluid patterns near the microrobots were recorded by a Zeiss AxioVert A1 TL/RL inverted microscope equipped with a Zeiss AxioCam 305 mono camera.

Drug Release from Microrobots: Drug release studies from the microrobots were performed in a 5 vol% DMSO solution in 1× PBS. First, 20000 drug-loaded microrobots per replicate were printed on a substrate and collected with 10 μL of the 5 vol% DMSO solution; the printed area was gently swiped with a pipette tip to release the particles from the substrate. The particle suspension was then aspirated and redispersed in 100 μL of the 5 vol% DMSO solution in a microcentrifuge tube. The particle suspension was gently agitated in a rotator at 37 °C. At each time point, the suspensions were centrifuged at 5000 × g, and supernatants were collected for measurement by a UV–vis spectrometer (Nanodrop 2000). The released drug was calculated by a calibration curve using the UV–vis absorbance values at 242 nm (Figure S8, Supporting Information). The particles were again redispersed in fresh 100 μL DMSO solution. This process was repeated until the cumulative drug release curve showed a plateau.

Acoustic Propulsion In Vitro: A silicone spacer (thickness = 0.5 mm, inner diameter = 10 mm) adhered to a glass slide was used as the fluidic chamber. To introduce an acoustic traveling wave to the chamber, a custom ceramic piezoelectric transducer and sensor (American Piezo), both with a resonant frequency of 1.3 MHz, were glued to the glass slide using a cyanoacrylate adhesive. Leads were soldered to the transducers and a sinusoidal AC signal was applied to the transducer by means of a function generator (33210A, Agilent) and amplifier (75A250AM2, Amplifier Research). The applied signal was monitored by an oscilloscope (DSOX1102G, Keysight). To investigate particle propulsion, the chamber was placed on a microscope stage (Nikon). A solution of microrobots in 1× PBS was gently pipetted into the fluidic chamber, and the transducer was stimulated using the conditions described in the Results section.

Isolation of Mouse Bladders and Acoustic Propulsion Ex Vivo: To investigate the propulsion and pinning of microrobots ex vivo, murine bladders were isolated from euthanized C57BL/6j mice, as previously described.^[80] Microrobots dispersed in 1× PBS were directly injected into the bladder immediately after isolation. The bladder was subsequently placed in the fluidic chamber and submerged in PBS before the application of the acoustic field. After applying the acoustic field for 5 min, the bladder was cut and transferred to a Petri dish filled with PBS. This timescale was chosen to give microrobots sufficient time to find the bladder wall. Due to the fast speed of the microrobots and their robust pinning, the long-term stability of the air bubble was not critical to maintain pinning. The cut bladder was washed by agitation in PBS with tweezers to simulate physiological shear stresses on epithelial cells in the bladder. Using scaling arguments, it was estimated that the shear stress (τ) experienced during washing was $\tau \approx \mu \frac{\Delta v}{\Delta y} \approx 7 \text{ dyn cm}^{-2}$, assuming i) that the viscosity (μ) of PBS was $8.9 \times 10^{-4} \text{ Pa s}$, ii) the velocity scale (Δv) was $\approx 8 \text{ cm s}^{-1}$ based on the washing procedure, and iii) the characteristic length (Δy) was 0.1 mm, which was $\approx 1/10$ th of the width of the bladder section. This was comparable to the $\approx 5 \text{ dyn cm}^{-2}$ shear stress typically experienced in the bladder during urination.^[81] This procedure was performed three times on each bladder. Then, the dried bladder was sputter-coated with platinum (thickness = 20 nm) to observe the location and orientation of pinned microrobots at the bladder wall using an SEM.

Characterization of the Frequency at Maximal Acoustic Response of the Air Bubble: To create a large chamber for characterizing the frequency at the maximal acoustic response of the air bubbles, 2000 particles were printed on a 2.5 cm × 2.5 cm glass substrate. A watertight chamber was assembled by affixing 2.5 cm × 2.5 cm glass walls around each side of the substrate with epoxy. A piezoelectric transducer was then affixed to the bottom of the substrate, adjacent to the printed particles (Figure S1, Supporting Information). To analyze the acoustic cavitation of the microrobots, returning pressure was converted into voltage via a 1 MHz unfocused piston (Olympus). The resulting voltage signals were collected over time using an InfiniiVision Oscilloscope (Agilent Technologies) at a 10 MHz sampling frequency with measurements starting immediately prior to initial sonication. Acoustic responses were collected for 11 frequencies (250–390 kHz). To determine the frequency at the maximal acoustic response of the air bubbles, data were analyzed using MATLAB (MathWorks). Voltage data was first cropped to remove any signal prior to the first expected return signal (round-trip travel time to the substrate). Tukey windowing was applied to the cropped signal to prevent spectral leakage on the fast Fourier transform (FFT). The FFT was then taken for every pulse, and the FFT magnitudes were averaged together within each frequency. Details on the computing harmonic cavitation dose are provided in the Supporting Information.

Numerical Simulations: COMSOL Multiphysics 6.0 was used to resolve the streaming flows around the microrobots upon excitation by ultrasound. A perturbation was applied in pressure and velocity to the Navier–Stokes equations. The zeroth order components were identified as quiescent fields, allowing to assume 0 as a value.^[53,82] The first-order components were identified as the oscillatory flows, and the time average of the second-order components was identified as the streaming flows. The acoustic actuation of the bubble was modeled with a sinusoidal Dirichlet boundary condition at the air/liquid interface.^[42] The first-order and second-order equations were simulated sequentially. The shape of the microrobot was placed in a cubic box with 100 μm edge lengths. Open boundaries were prescribed on the surfaces of the box. The first-order fields were solved over one period of oscillation using the time-dependent Stokes solver. The time-averaged second-order equations were solved using a steady Stokes solver. The non-linear term was calculated by time-averaging the first-order fields and was included as a body force in the time-averaged second-order equations. A detailed description of the design of the numerical simulations is provided in the Supporting Information. Simulated time-averaged second-order velocity streamlines and pressure fields are reported in Figure 3 without the inclusion of quiescent or first-order pressure fields.

Murine Bone Marrow Isolation: Macrophages were isolated from murine bone marrow using methods described previously.^[83] Briefly, 8- to 10-week-old male C57BL/6j mice (Jackson Laboratory) were euthanized by CO₂ inhalation followed by cervical dislocation. Tibias and femurs were isolated using a sterile scalpel and scissors. After removing the muscles and tendons, the bones were rinsed with 70% ethanol, rinsed again with Dulbecco’s phosphate-buffered saline (DPBS, Cytiva), and stored in DPBS at 4 °C until use. In sterile conditions, the epiphysis of femurs and tibias were removed by cutting, and the bone marrow was flushed out with DPBS at 4 °C using a 30-gauge needle. The isolated bone marrow cells were filtered through a 40-μm cell strainer to remove large aggregates. Cells were resuspended in a Bamberker freezing medium (GC Lymphotech Inc.) and stored in liquid nitrogen until further use. All centrifugations associated with cells in this study were performed at 350 × g for 5 min at 4 °C.

Culture of Primary Macrophages from Murine Bone Marrow: Bone marrow-derived macrophages (BMDMs) were differentiated from murine bone marrow progenitor cells using previously described methods.^[83] Briefly, 8 million bone marrow cells were thawed and mixed with bone marrow media (BMM–; i.e., 50 mL of fetal bovine serum [FBS] (Thermo Fisher Scientific), 5 mL of Pen Strep solution (Cytiva), and 25 mL of GlutaMAX Supplement (Thermo Fisher Scientific) in 500 mL of DMEM/F-12 (Thermo Fisher Scientific) at a volume ratio of 1:5). Cells were centrifuged and aspirated, resuspended in BMM+ (i.e., 20 ng of recombinant murine macrophage-colony stimulating factor (M-CSF,

ProTech) per mL of BMM–), and added to a non-treated T175 flask (Corning) filled to a final volume of 25 mL BMM+. After incubating the cells for 3 days, an additional 25 mL of BMM+ was added. Once the cells reached 70% confluency (typically after 10 total days of incubation), the media was aspirated, adherent cells were washed with DPBS, and 15 mL of 4 °C Accumax (Innovative Cell Technologies Inc.) was added to the flask. Cells were incubated for 10 min, vigorously agitated by thumping, and an additional 10 mL of Accumax was added. After an additional 10 min of incubation, the flask was thumped again to dislodge the remaining cells, and the suspension of BMDMs was transferred to a 50 mL conical tube. An equal volume of BMM– was added into the tube to deactivate the Accumax, and the BMDM suspension was centrifuged. Cells were resuspended in BMM+ for further use. All cell incubations performed in this study were at 37 °C and 5% CO₂.

In Vitro BMDM Inflammatory Response and Cellular Phenotyping: To measure the response of BMDMs to drugs released from the microrobots, cells were seeded in a 96-well plate at 10000 cells per well in 100 µL of DMEM (Cytiva) and incubated for 24 h. Wells were washed with DPBS and 200 µL of DMEM containing 20 ng of LPS was added to each well to initiate an inflammatory response. After 24 h, each well was washed with DPBS, and 200 µL of DMEM containing ≈4000 DEX-encapsulating microrobots or pure DMEM was added to each well. The number of added microrobots was determined by calculating the drug loading capacity of each microrobot ($\approx 5 \times 10^{-12}$ g of DEX) from the drug release profile. To reach 100 nM of DEX concentration in 48 h to polarize M1-like macrophages toward M2 phenotypes, microrobots needed to release at least $\approx 1.6 \times 10^{-8}$ g of DEX. After 24 or 48 h of incubation, BMDMs were collected from each well using Accumax. After collection, BMDMs were stained with anti-CD86, anti-MHC II, anti-iNOS, anti-CD206, and anti-Arg1 antibodies for inspection by flow cytometry. The complete protocol for cellular phenotyping is provided in the Supporting Information.

Supporting Information

Supporting Information is available from the Wiley Online Library or from the author.

Acknowledgements

The authors thank Taylor Ausec (CU Boulder) for helpful discussions and Dylan Bartusiak (CU Boulder) for access to the cleanroom. This work was supported by a National Science Foundation (NSF) CAREER grant (CBET 2143419), the National Institutes of Health (NIH R21AI154266 and R35GM147455), and the Office of Naval Research (ONR N000142212541). C.W.S. is a Pew Scholar in the Biomedical Sciences, supported by the Pew Charitable Trusts. C.W.S. would also like to thank the Packard Foundation for their support of this project. N.B.D. was funded by the Teets Family Endowed Doctoral Fellowship in Nanotechnology. The authors also thank the Colorado Shared Instrumentation in Nanofabrication and Characterization (COSINC) for use of their instrumentation. Some of the figures in this manuscript were made using BioRender.com.

Conflict of Interest

The authors declare no conflict of interest.

Data Availability Statement

The data that support the findings of this study are available in the supplementary material of this article.

Keywords

acoustic field, drug delivery, microrobots, self-propelling particles

Received: January 14, 2023

Revised: March 14, 2023

Published online:

- [1] C. W. Shields, L. L. Wang, M. A. Evans, S. Mitragotri, *Adv. Mater.* **2020**, *32*, 1901633.
- [2] J. G. Lee, K. Lannigan, W. A. Shelton, J. Meissner, B. Bharti, *Langmuir* **2020**, *36*, 14157.
- [3] D. S. Spencer, A. S. Puranik, N. A. Peppas, *Curr. Opin. Chem. Eng.* **2015**, *7*, 84.
- [4] M. J. Mitchell, M. M. Billingsley, R. M. Haley, M. E. Wechsler, N. A. Peppas, R. Langer, *Nat. Rev. Drug Discovery* **2021**, *20*, 101.
- [5] D. Peer, J. M. Karp, S. Hong, O. C. Farokhzad, R. Margalit, R. Langer, *Nat. Nanotechnol.* **2007**, *2*, 751.
- [6] V. Sharma, E. Azar, A. P. Schroder, C. M. Marques, A. Stocco, *Soft Matter* **2021**, *17*, 4275.
- [7] W. I. Hagens, A. G. Oomen, W. H. de Jong, F. R. Cassee, A. J. A. M. Sips, *Regul. Toxicol. Pharmacol.* **2007**, *49*, 217.
- [8] H. Al-Obaidi, A. T. Florence, *J. Drug Delivery Sci. Technol.* **2015**, *30*, 266.
- [9] S. Wilhelm, A. J. Tavares, Q. Dai, S. Ohta, J. Audet, H. F. Dvorak, W. C. W. Chan, *Nat. Rev. Mater.* **2016**, *1*, 16014.
- [10] G. A. Rance, D. H. Marsh, S. J. Bourne, T. J. Reade, A. N. Khlobystov, *ACS Nano* **2010**, *4*, 4920.
- [11] A. Subrizi, E. M. del Amo, V. Korzhikov-Vlakh, T. Tennikova, M. Ruponen, A. Urtti, *Drug Discovery Today* **2019**, *24*, 1446.
- [12] E. Lauga, W. R. DiLuzio, G. M. Whitesides, H. A. Stone, *Biophys. J.* **2006**, *90*, 400.
- [13] B. Liu, M. Gulino, M. Morse, J. X. Tang, T. R. Powers, K. S. Breuer, *Proc. Natl. Acad. Sci. U. S. A.* **2014**, *111*, 11252.
- [14] R. Nosrati, A. Driouchi, C. M. Yip, D. Sinton, *Nat. Commun.* **2015**, *6*, 8703.
- [15] P. P. Lele, T. Roland, A. Shrivastava, Y. Chen, H. C. Berg, *Nat. Phys.* **2016**, *12*, 175.
- [16] A. Persat, C. D. Nadell, M. K. Kim, F. Ingremeau, A. Siryaporn, K. Drescher, N. S. Wingreen, B. L. Bassler, Z. Gitai, H. A. Stone, *Cell* **2015**, *161*, 988.
- [17] Z. Wu, Y. Chen, D. Mukasa, O. S. Pak, W. Gao, *Chem. Soc. Rev.* **2020**, *49*, 8088.
- [18] F. Zhang, J. Zhuang, Z. Li, H. Gong, B. E.-F. de Ávila, Y. Duan, Q. Zhang, J. Zhou, L. Yin, E. Karshalev, W. Gao, V. Nizet, R. H. Fang, L. Zhang, J. Wang, *Nat. Mater.* **2022**, *21*, 1324.
- [19] C. Gao, Y. Feng, D. A. Wilson, Y. Tu, F. Peng, *Small* **2022**, *18*, 2106263.
- [20] V. Sridhar, F. Podjaski, Y. Alapan, J. Kröger, L. Grunenberg, V. Kishore, B. V. Lotsch, M. Sitti, *Sci. Robot.* **2022**, *7*, eabm1421.
- [21] N. L. Abbott, O. D. Velev, *Curr. Opin. Colloid Interface Sci.* **2016**, *21*, 1.
- [22] C. W. Shields, O. D. Velev, *Chem* **2017**, *3*, 539.
- [23] K. Han, C. W. Shields, O. D. Velev, *Adv. Funct. Mater.* **2018**, *28*, 1705953.
- [24] A. al Harraq, B. D. Choudhury, B. Bharti, *Langmuir* **2022**, *38*, 3001.
- [25] A. Ganguly, A. Gupta, *Phys. Rev. Fluids* **2023**, *8*, 014103.
- [26] K. K. Dey, F. Wong, A. Altemose, A. Sen, *Curr. Opin. Colloid Interface Sci.* **2016**, *21*, 4.
- [27] A. M. Brooks, M. Tasinkevych, S. Sabrina, D. Velegol, A. Sen, K. J. M. Bishop, *Nat. Commun.* **2019**, *10*, 495.
- [28] M. B. Akolpoglu, Y. Alapan, N. O. Dogan, S. F. Baltaci, O. Yasa, G. Aybar Tural, M. Sitti, *Sci. Adv.* **2022**, *8*, eabo6163.

- [29] Z. Wu, J. Troll, H.-H. Jeong, Q. Wei, M. Stang, F. Ziemssen, Z. Wang, M. Dong, S. Schnichels, T. Qiu, P. Fischer, *Sci. Adv.* **2018**, 4, eaat4388.
- [30] C. C. J. Alcántara, S. Kim, S. Lee, B. Jang, P. Thakolkaran, J. Kim, H. Choi, B. J. Nelson, S. Pané, *Small* **2019**, 15, 1805006.
- [31] R. Maria-Hormigos, C. C. Mayorga-Martinez, M. Pumera, *Small* **2022**, 2204887.
- [32] T. Gwisai, N. Mirkhani, M. G. Christiansen, T. T. Nguyen, V. Ling, S. Schuerle, *Sci Robot* **2022**, 7, eabo0665.
- [33] S. Gangwal, O. J. Cayre, M. Z. Bazant, O. D. Velev, *Phys. Rev. Lett.* **2008**, 100, 058302.
- [34] J. G. Lee, A. M. Brooks, W. A. Shelton, K. J. M. Bishop, B. Bharti, *Nat. Commun.* **2019**, 10, 2575.
- [35] Z. Wang, Z. Wang, J. Li, S. T. H. Cheung, C. Tian, S.-H. Kim, G.-R. Yi, E. Ducrot, Y. Wang, *J. Am. Chem. Soc.* **2019**, 141, 14853.
- [36] C. P. Thome, W. S. Hoerl, J. R. Bendorf, J. G. Lee, C. W. Shields, *Nano Lett.* **2023**, 23, 2379.
- [37] A. Aghakhani, O. Yasa, P. Wrede, M. Sitti, *Proc. Natl. Acad. Sci. U. S. A.* **2020**, 117, 3469.
- [38] T. Luo, M. Wu, *Lab Chip* **2021**, 21, 4095.
- [39] J.-F. Louf, N. Bertin, B. Dollet, O. Stephan, P. Marmottant, *Adv. Mater. Interfaces* **2018**, 5, 1800425.
- [40] K. J. Rao, F. Li, L. Meng, H. Zheng, F. Cai, W. Wang, *Small* **2015**, 11, 2836.
- [41] L. Ren, F. Soto, L. Huang, W. Wang, in *Field-Driven Micro and Nanorobots for Biology and Medicine*, Springer International Publishing, Springer, New York **2022**, pp. 29–60.
- [42] N. Bertin, T. A. Spelman, O. Stephan, L. Gredy, M. Bouriau, E. Lauga, P. Marmottant, *Phys. Rev. Appl.* **2015**, 4, 064012.
- [43] L. Ren, N. Nama, J. M. McNeill, F. Soto, Z. Yan, W. Liu, W. Wang, J. Wang, T. E. Mallouk, *Sci. Adv.* **2019**, 5, eaax3084.
- [44] S. Fusco, F. Ullrich, J. Pokki, G. Chatzipiripiridis, B. Özkale, K. M. Sivaraman, O. Ergeneman, S. Pané, B. J. Nelson, *Expert Opin. Drug Delivery* **2014**, 11, 1815.
- [45] N. Tanjeem, M. B. Minnis, R. C. Hayward, C. W. Shields, *Adv. Mater.* **2022**, 34, 2105758.
- [46] R. A. Henry, A. Morales, C. M. Cahill, *Urology* **2015**, 85, 1025.
- [47] Y. Homma, Y. Akiyama, H. Tomoe, A. Furuta, T. Ueda, D. Maeda, A. T. Lin, H. Kuo, M. Lee, S. Oh, J. C. Kim, K. Lee, *Int. J. Urol.* **2020**, 27, 578.
- [48] W. F. Rawls, L. Cox, E. S. Rovner, *NeuroUrol. Urodyn.* **2017**, 36, 1677.
- [49] R. Hajjo, D. A. Sabbah, S. K. Bardaweel, *ACS Omega* **2020**, 5, 29765.
- [50] J. M. McNeill, N. Nama, J. M. Braxton, T. E. Mallouk, *ACS Nano* **2020**, 14, 7520.
- [51] M. Lanoy, C. Derec, A. Tourin, V. Leroy, *Appl. Phys. Lett.* **2015**, 107, 214101.
- [52] M. Kaynak, A. Ozcelik, A. Nourhani, P. E. Lammert, V. H. Crespi, T. J. Huang, *Lab Chip* **2017**, 17, 395.
- [53] N. Nama, R. Barnkob, Z. Mao, C. J. Kähler, F. Costanzo, T. J. Huang, *Lab Chip* **2015**, 15, 2700.
- [54] N. Nama, P.-H. Huang, T. J. Huang, F. Costanzo, *Biomechanics* **2016**, 10, 024124.
- [55] D. Ahmed, T. Baasch, B. Jang, S. Pane, J. Dual, B. J. Nelson, *Nano Lett.* **2016**, 16, 4968.
- [56] Y.-S. Tung, J. J. Choi, B. Baseri, E. E. Konofagou, *Ultrasound Med. Biol.* **2010**, 36, 840.
- [57] P. Sharan, Z. Xiao, V. Mancuso, W. E. Uspal, J. Simmchen, *ACS Nano* **2022**, 16, 4599.
- [58] X. Wang, J. Cai, L. Sun, S. Zhang, D. Gong, X. Li, S. Yue, L. Feng, D. Zhang, *ACS Appl. Mater. Interfaces* **2019**, 11, 4745.
- [59] H. Ito, A. E. Pickering, Y. Igawa, A. J. Kanai, C. H. Fry, M. J. Drake, *Front. Physiol.* **2017**, 8, 49.
- [60] N. B. Day, W. C. Wixson, C. W. Shields, *Acta Pharm. Sin. B* **2021**, 11, 2172.
- [61] R. Sangsuwan, J. H. N. Yik, M. Owen, G.-Y. Liu, D. R. Haudenschild, J. S. Lewis, *Acta Biomater.* **2022**, 149, 347.
- [62] M. A. Zieringer, N. J. Carroll, A. Abbaspourrad, S. A. Koehler, D. A. Weitz, *Small* **2015**, 11, 2903.
- [63] Y. K. Jo, D. Lee, *Small* **2020**, 16, 1903736.
- [64] S. S. Datta, A. Abbaspourrad, E. Amstad, J. Fan, S.-H. Kim, M. Romanowsky, H. C. Shum, B. Sun, A. S. Utada, M. Windbergs, S. Zhou, D. A. Weitz, *Adv. Mater.* **2014**, 26, 2205.
- [65] I. Permanadewi, A. C. Kumoro, D. H. Wardhani, N. Aryanti, *J. Phys. Conf. Ser.* **2019**, 1295, 012063.
- [66] S. Jana, A. Saha, A. K. Nayak, K. K. Sen, S. K. Basu, *Colloids Surf., B* **2013**, 105, 303.
- [67] N. B. Day, R. Dalhuisen, N. E. Loomis, S. G. Adzema, J. Prakash, C. W. Shields IV, *Acta Biomater.* **2022**, 150, 211.
- [68] P. J. Murray, *Annu. Rev. Physiol.* **2017**, 79, 541.
- [69] T. Lawrence, G. Natoli, *Nat. Rev. Immunol.* **2011**, 11, 750.
- [70] A. Viola, F. Munari, R. Sánchez-Rodríguez, T. Scolaro, A. Castegna, *Front. Immunol.* **2019**, 10.
- [71] C. Atri, F. Guerfali, D. Laouini, *Int. J. Mol. Sci.* **2018**, 19, 1801.
- [72] T. Quante, Y. C. Ng, E. E. Ramsay, S. Henness, J. C. Allen, J. Parmentier, Q. Ge, A. J. Ammit, *Am. J. Respir. Cell Mol. Biol.* **2008**, 39, 208.
- [73] M. J. Ratcliffe, I. G. Dougall, *BMC Pharmacol. Toxicol.* **2012**, 13, 15.
- [74] A. Higham, T. Scott, J. Li, R. Gaskell, A. B. Dikwa, R. Shah, M. A. Montero-Fernandez, S. Lea, D. Singh, *Clin. Sci.* **2020**, 134, 751.
- [75] A.-A. Martí i Llinde, W. Reith, *Cell. Mol. Life Sci.* **2021**, 78, 5303.
- [76] T. Limongi, L. Brigo, L. Tirinato, F. Pagliari, A. Gandin, P. Contessotto, A. Giugni, G. Brusatin, *Biomed. Mater.* **2021**, 16, 035013.
- [77] M. Nouri-Goushki, A. Sharma, L. Sasso, S. Zhang, B. C. J. Van der Eerden, U. Staufer, L. E. Fratila-Apachitei, A. A. Zadpoor, *ACS Biomater. Sci. Eng.* **2019**, 5, 6127.
- [78] W. Wang, T. E. Mallouk, *ACS Nano* **2021**, 15, 15446.
- [79] C. A. Schneider, W. S. Rasband, K. W. Eliceiri, *Nat. Methods* **2012**, 9, 671.
- [80] M. Charni-Natan, I. Goldstein, *STAR Protoc.* **2020**, 1, 100086.
- [81] D. Maggiorani, R. Dissard, M. Belloy, J.-S. Saulnier-Blache, A. Casemayou, L. Ducasse, S. Grès, J. Bellière, C. Caubet, J.-L. Bascands, J. P. Schanstra, B. Buffin-Meyer, *PLoS One* **2015**, 10, e0131416.
- [82] P. B. Muller, R. Barnkob, M. J. H. Jensen, H. Bruus, *Lab Chip* **2012**, 12, 4617.
- [83] C. W. Shields, M. A. Evans, L. L.-W. Wang, N. Baugh, S. Iyer, D. Wu, Z. Zhao, A. Pusuluri, A. Ukidve, D. C. Pan, S. Mitragotri, *Sci. Adv.* **2020**, 6, eaaz6579.